

# Determining magnetization configurations and reversal of individual magnetic nanotubes

17

*M. Poggio*

Department of Physics, University of Basel, Basel, Switzerland

## 17.1 Introduction

### 17.1.1 Magnetic nanostructures

The study of magnetic nanostructures is motivated both by fundamental questions about the effects of miniaturization on magnetic properties and by their potential applications. Nanometer-scale magnets can be used as elements in dense magnetic memories, logical devices [1], and magnetic sensors [2] and as probes in high-resolution imaging applications [3–5]. For applications, such as dense magnetic storage or high-resolution sensing, there is clear motivation to reduce element size as much as possible. At the same time, however, to be useful, magnetic elements must have both well-defined remnant states and reproducible reversal processes.

As element size continues to shrink, these requirements become increasingly difficult to meet. The intrinsically large surface-to-volume ratio of nanometer-scale magnets makes their magnetization configurations especially susceptible to roughness and exterior imperfections. Furthermore, the presence of surface and edge domains can lead to complicated switching processes that are slow and not reproducible [6,7]. Near borders, magnetization tends to change direction to minimize stray-field energy. As a result, the form of surfaces and edges—including any imperfections or roughness—determines the configuration of the magnetization in their vicinity. The resulting magnetization inhomogeneities affect reversal by acting as potential nucleation sites for complex switching processes [8–12]. Furthermore, small differences in the initial configurations of edge and surface domains can lead to entirely different reversal modes, complicating the control and reproducibility of magnetic switching from nanomagnet to nanomagnet [6].

Although, in practice, the effect of roughness can never be completely eliminated, one way to reduce the influence of edges and surfaces on magnetic reversal is to use magnetic structures that support flux-closure magnetization configurations [13]. Since these configurations minimize stray field, edges and surfaces play a lesser role in determining both their equilibrium state and their dynamics than for nonflux-closure configurations. As a result, structures hosting flux-closure configurations should favor stable remnant states and both fast and reproducible reversal processes. In addition, the lack of stray field produced by flux-closure configurations suppresses interactions

between nearby nanomagnets. This property is potentially useful for the design of closely packed arrays, for example, as in a high-density memory. Nevertheless, a minimum element size is imposed by the stability of flux-closure configurations, which requires an element size significantly larger than the dipolar exchange length [14].

On the nanometer-scale, core-free geometries such as rings [11,15] and tubes [16] have been proposed as hosts of vortex-like flux-closure configurations with magnetization pointing along their circumference. Such configurations owe their stability to the minimization of magnetostatic energy at the expense of exchange energy. Crucially, the lack of a magnetic core removes the dominant contribution to the exchange energy, which otherwise compromises the stability of vortex states.

### 17.1.2 Ferromagnetic nanotubes

In this chapter, we focus on ferromagnetic nanotubes (FNTs) and their experimental investigation by techniques capable of measuring the response of individual specimens. This capability has developed recently and is now having a strong impact on our understanding of the behavior of real FNT structures. For more general treatments, including discussion of their fabrication and measurements mostly of large ensembles of FNTs, we point the reader to Chapters 14 and 31 of *Handbook of Nanophysics: Nanotubes and Nanowires* [17], a review by Sousa et al. [18], and Chapter 24 of this book. Chapter 3 of *Handbook of Magnetic Materials* [19] provides the most recent comprehensive review of the topic, just to the point at which measurements started to shift from ensembles to individual elements.

At equilibrium, the hollow magnetic geometry of FNTs is expected to stabilize vortex-like flux-closure configurations with magnetization pointing along the FNT circumference. Although vortex configurations have been observed localized at the ends of ferromagnetic nanowires (FNWs) [20], the exchange energy penalty for the magnetic singularity along the vortex axis tends to favor nonflux-closure states. In a FNT the lack of this axial Bloch point structure [21] is also expected to allow for fast magnetization reversal that begins with vortices nucleating at its ends and propagating along its length [16,22,23]. Due to their tubular geometry, FNTs may reveal curvature-induced effects [24,25], such as asymmetric spin-wave dispersion [26] or Cherenkov-type emission of magnons by certain types of domain walls [27]. Theoretical studies of magnetization configurations in ferromagnetic FNTs have predicted an equilibrium flux-closure configuration, the so-called global vortex state, and other configurations, including a uniform axial state and a mixed state [16]. In a global vortex state, the entire FNT's magnetization is circumferentially aligned, while the mixed state combines vortex-like ends, minimizing magnetostatic energy, and an axially aligned center, minimizing exchange energy. Calculations suggest that for short FNTs, opposing vortex states, in which two vortices with opposing circulation are separated by a Néel domain wall, may also be stable [28]. The dependence of the FNT's equilibrium magnetization configuration on geometry and details such as the relative sense of circulation of the end vortices have been considered both analytically and numerically [28–30]. In particular, it has been predicted that the global vortex state can be programmed as the stable remnant configuration by a small FNT length-to-diameter ratio (Fig. 17.1).

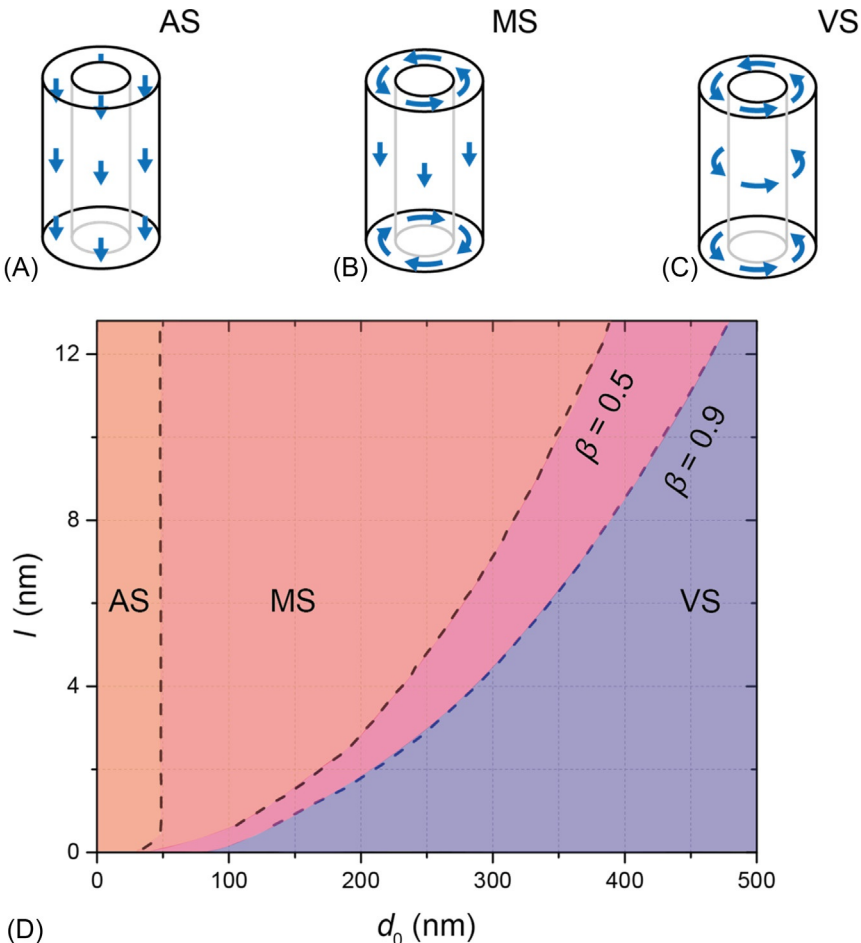


**Fig. 17.1** Possible equilibrium magnetization configurations are illustrated: (A) axial state (AS), (B) mixed state (MS), and (C) vortex state (VS). Magnetic phase diagram as a function of FNT diameter ( $d_0$ ) and length ( $l$ ). The MS-V transition is shown for two different shape factors  $\beta = 0.5$  and  $\beta = 0.9$ , where  $\beta$  is the ratio of the inner and outer FNT diameter.

Adapted from P. Landeros, O.J. Suarez, A. Cuchillo, P. Vargas, Phys. Rev. B 79 (2009) 024404.

### 17.1.3 Measuring assemblies versus individual magnetic nanotubes

Despite the wealth of predictions on the equilibrium configurations and reversal modes of FNTs, direct experimental evidence of their magnetic behavior has emerged only recently. This is partly due to the difficulty of measuring individual magnetic nanostructures with many conventional magnetometry techniques, which do not have the necessary sensitivity to detect the small total magnetic moment of a single nanomagnet. As a result, measurements of their magnetic properties are often carried out on large ensembles [31–37], whose constituent nanomagnets have a distribution of

size, shape, and orientation and—depending on the density—may interact with each other [31,38]. These complications conspire to make accurate characterization of the stable magnetization configurations and reversal processes difficult.

To obtain a clear understanding of the magnetic properties of FNTs, it is therefore advantageous to investigate individual specimens. In the following sections, we review such efforts. In a pioneering work carried out in 1996, Wernsdorfer et al. [39] investigated the magnetic reversal of an individual Ni nanowire at 4 K using a miniaturized superconducting quantum interference device (SQUID). Detecting the stray magnetic flux  $\Phi$  from one end of the nanowire as a function of magnetic field  $H$ ,  $\Phi$  was assumed to be approximately proportional to the projection of the total magnetization  $M$  along the nanowire axis. At the time,  $M(H)$  of the individual nanowire was not accessible, and micromagnetic simulations were conducted only a decade later [40].

These micrometer-scale SQUID measurements of single FNWs were followed by other measurements of individual FNWs by electron holography [41], magnetic force microscopy (MFM) [42,43], magnetotransport [44–48], and X-ray microscopy [49]. Magnetization configurations of individual rolled-up ferromagnetic membranes between 2 and 16  $\mu\text{m}$  in diameter were also imaged using the optical Kerr effect [50] and X-ray microscopy [50–52]. In these studies, the authors reported azimuthal domain patterns that were commensurable throughout the windings and attributed the effect to magnetostatic [52,53] or exchange [50] coupling between windings. In the following, we focus on magnetic configurations in individual FNTs, which are an order of magnitude smaller. These FNTs are prepared as continuous magnetic shells around nanotemplates, allowing for both magnetostatic and exchange coupling.

## 17.2 Magnetoresistance

Measurements of magnetoresistance (MR) monitor the change in electrical resistance of a sample as a function of the applied external magnetic field. Through the anisotropic magnetoresistance (AMR) effect, whose fundamental origin is spin-flip scattering due to spin-orbit coupling, the measured resistance can then be related to the magnetization orientation in the sample. As a result, by electrically contacting an individual FNT, measurements of its integrated magnetization can be made.

Early MR measurements of individual FNTs were carried out by Zhang et al. in 2004 on  $\text{Fe}_3\text{O}_4$  FNTs grown on MgO NW templates [54]. Subsequent measurements of MnAs FNTs by Liang et al. in 2012 [55] and of GaMnAs FNTs by Butschkow et al. in 2013 [56] provided more detailed information on the magnetization reversal. In both cases, core-shell NWs consisting of a hexagonal GaAs core and a MnAs or GaMnAs shell were grown by molecular beam epitaxy (MBE). The nonmagnetic semiconductor cores and the ferromagnetic semiconductor shells together formed FNTs. Single FNTs were isolated on an insulating substrate and metallic electrodes were patterned to make ohmic contact to each FNT. Transport measurements were then carried out in four-terminal configuration at cryogenic temperatures and in applied magnetic fields. As observed in the MR measurements, the magnetization

behavior in this type of FNTs is dominated by magnetocrystalline anisotropy of the material itself rather than the shape anisotropy of the tube. As a result, vortex-like flux-closure states are not supported in these samples, and no experimental evidence for their presence was found in either experiment.

In an effort to favor the formation of vortex states and measure their presence in a single FNT, starting in 2012, researchers focused on FNTs made from polycrystalline or amorphous materials with nearly isotropic magnetic properties. Rüffer et al. performed MR measurements on single metallic FNTs formed by a 40-nm layer of Ni deposited by atomic layer deposition (ALD) on GaAs NWs with a hexagonal cross section [57]. As in previous measurements, the GaAs NWs served as nonmagnetic templates, this time for the polycrystalline Ni film, which—in contrast to MnAs and GaMnAs—does not exhibit magnetocrystalline anisotropy. These FNTs had an outer width of 150 nm and lengths of 20  $\mu\text{m}$ . Four-terminal MR measurements of individual FNTs were performed as a function of applied magnetic field both parallel and perpendicular to the FNT axis (Fig. 17.2). The results were consistent with the presence of vortex-like magnetization configurations near remanence. The authors suggested a number of possible low-field magnetization configurations to explain their results, including a multidomain vortex state, consisting of segments of azimuthally oriented magnetization separated by axial domain wall; an onion state, consisting of two sections of oppositely oriented azimuthal magnetization separated by axial walls; and a global vortex state, in which the magnetization of the entire FNT is

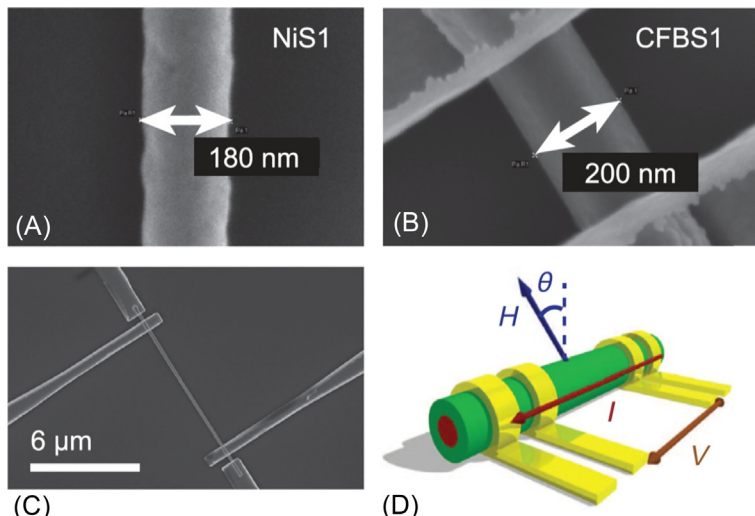


**Fig. 17.2** Scanning electron microscopy images of a small segment of (A) Ni FNT and (B) CoFeB FNT. (C) Overview of sample CoFeB FNT with electrical contacts. (D) MR measurement configuration.

Adapted from D. Rüffer, M. Slot, R. Huber, T. Schwarze, F. Heimbach, G. Tütüncüoglu, F. Matteini, E. Russo-Averchi, A. Kovács, R. Dunin-Borkowski, R.R. Zamani, J.R. Morante, J. Arbiol, A.F.i. Morral, D. Grundler, *APL Mater.* 2 (2014) 076112.

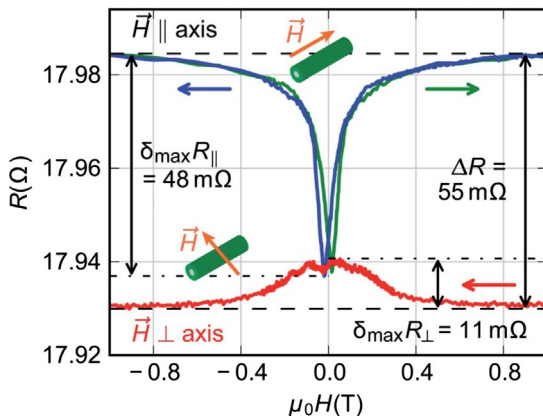


**Fig. 17.3** Resistance of a 10-mm-long Ni FNT segment for magnetic field  $H$  sweeps in positive (green) and negative (blue) directions when  $H$  is parallel to the long axis (upper curves). The magnetoresistance is hysteretic and positive at large fields. For  $H$  perpendicular to the long axis, the magnetoresistance is negative to large fields.

Adapted from D. Rüffer, R. Huber, P. Berberich, S. Albert, E. Russo-Averchi, M. Heiss, J. Arbiol, A.F.i. Morral, D. Grundler, *Nanoscale* 4 (2012) 4989.

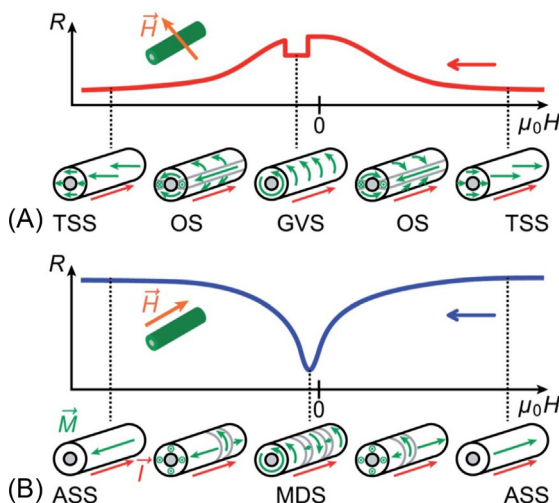


**Fig. 17.4** Magnetic states schematically attributed to characteristic  $r$  resistance values in (A) a perpendicular and (B) a parallel magnetic field.

Adapted from D. Rüffer, R. Huber, P. Berberich, S. Albert, E. Russo-Averchi, M. Heiss, J. Arbiol, A.F.i. Morral, D. Grundler, *Nanoscale* 4 (2012) 4989.

oriented along one azimuthal direction (Figs. 17.3 and 17.4). Although the lack of magnetocrystalline anisotropy allowed for vortex-like magnetization configurations, the surface roughness of the Ni FNTs and their jagged or spherical ends likely

precluded the observation of the magnetization configurations and reversal modes predicted for idealized tubes.

Later, many of the same authors also investigated similar FNTs with CoFeB and Ni<sub>80</sub>Fe<sub>20</sub> (permalloy) shells. Amorphous CoFeB FNTs were produced by magnetron sputtering onto the GaAs template NWs [58], while polycrystalline Ni<sub>80</sub>Fe<sub>20</sub> FNTs were deposited by thermal evaporation [59]. Baumgaertl et al. carried out MR measurements relying on both the AMR effect and the anomalous Nernst effect combined with a focused laser beam to produce local temperature gradients within the FNTs [59]. The results suggested that the Ni<sub>80</sub>Fe<sub>20</sub> FNTs prefer an axially aligned magnetization configuration and that reversal occurs via a vortex domain wall. On the other hand, the CoFeB FNTs showed evidence for a remanent configuration with partly azimuthally aligned magnetization, probably stabilized by a growth-induced magnetic anisotropy [60].

In 2018, Zimmermann et al. did MR of individual Ni<sub>80</sub>Fe<sub>20</sub> FNTs, which—together with X-ray microscopy images—showed clear MR signal consistent with the presence of remanent vortex states [61]. These results are discussed in further detail in Section 6, where we review X-ray microscopy of FNTs.

## 17.3 Torque magnetometry

In 2012, researchers started applying sensitive torque magnetometry to measure magnetic hysteresis of individual FNTs. The first such experiments were carried out by Weber et al. [62] on the polycrystalline Ni FNTs studied earlier by Rüffer et al. [57]. The researchers used a technique known as dynamic cantilever magnetometry (DCM), which measures the curvature of a sample's free energy  $E_m$  with respect to the magnetic field orientation [63–67]. The high sensitivity provided by the ultrasoft Si cantilevers used as torque transducers allows for the measurement of individual nanomagnets [68–70], as well as other nanostructures producing a magnetic response [71–73]. Measurements require the FNT of interest to be attached to a cantilever transducer, whose mechanical resonance frequency  $f$  is monitored as a function of the applied external magnetic field  $\mathbf{H}$ . The frequency shift  $\Delta f = f - f_0$ , where  $f_0$  is the frequency at  $H = 0$  is given by

$$\Delta f = \frac{f_0}{2k_0 l_e^2} \left( \frac{\partial^2 E_m}{\partial \theta_c^2} \Big|_{\theta_c=0} \right)$$

where  $k_0$  is the cantilever spring constant,  $l_e$  its effective length, and  $\theta_c$  its angle of oscillation [66,69] (Fig. 17.5).

Initial measurements on Ni FNTs were conducted in three different field orientations and provided evidence for the presence of multidomain states and onion states near remanence. These results were consistent with earlier MR measurements by Rüffer et al. on the same set of samples, in which the presence of a remanent global vortex state was not unambiguously observed. Again, sample roughness and

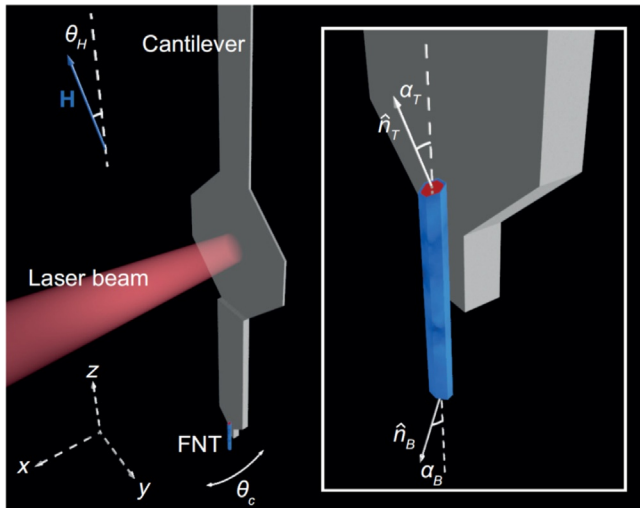


**Fig. 17.5** Schematic diagram of the DCM measurement: Si cantilever (gray) and CoFeB FNT (blue) with GaAs core (red). The cantilever oscillates about  $\hat{y}$ , and the FNT axis is parallel to  $\hat{z}$ . The applied magnetic field  $H$  can be rotated in the  $xz$ -plane by an angle  $\theta_c$  with respect to  $\hat{z}$ . The unit vector  $\hat{n}_T$  ( $\hat{n}_B$ ) defines a perpendicular plane, in which the top (bottom) end of the FNT lies. The angle  $\alpha_T$  ( $\alpha_B$ ) refers to the angle of this vector with respect to the FNT axis  $\hat{z}$ .  
Adapted from A. Mehlin, B. Gross, M. Wyss, T. Schefer, G. Tütüncüoglu, F. Heimbach, A.F.i. Morral, D. Grundler, M. Poggio, Phys. Rev. B 97 (2018) 134422.

imperfections likely prevented such idealized states from being the equilibrium magnetization configurations. The measurements also yielded the value for the saturation magnetization of the FNTs, which was equal, within the experimental error, to the value known for bulk crystalline Ni.

Follow-up measurements of these Ni FNTs by Buchter et al. [74] and Nagel et al. [75] combined DCM with a nanometer-scale superconducting quantum interference device (nanoSQUID), which was used to measure the magnetic flux originating from the end of an individual FNT. This combination allowed the researchers to simultaneously monitor a single FNT's volume magnetization, by DCM, and the stray field produced by one of its ends, by nanoSQUID. The difference between the magnetic hysteresis curves measured by DCM and nanoSQUID and comparison with micromagnetic simulations indicated that the magnetization reversal process—at least in the measured FNT—did not start from the end closest to the nanoSQUID, but rather from a remote segment. This result contradicted the theoretical literature on the reversal of an ideal FNT, in which magnetization reversal is predicted to start with the appearance of vortex configurations at the two ends. Once again, this deviation from ideal behavior was likely due to the roughness of the Ni FNT and the imperfection of its ends.

In 2015, many of the same authors carried out similar DCM/nanoSQUID measurements of the  $\text{Ni}_{80}\text{Fe}_{20}$  FNTs previously measured using MR by Baumgaertl et al. [76]. In contrast to the measurements of single Ni FNTs, comparison between DCM and nanoSQUID signal from individual  $\text{Ni}_{80}\text{Fe}_{20}$  FNTs indicated that magnetization

reversal in these nanomagnets—in the absence of exchange bias coupling—did indeed follow the predicted behavior. Measurements were consistent with a reversal that proceeded through the nucleation of vortex configurations at the ends of the FNT followed by an irreversible switching process. These FNTs were made from 30-nm-thick thermally evaporated shell of Ni<sub>80</sub>Fe<sub>20</sub> on a GaAs NW template. They were 10–20 μm long with 150-nm-wide hexagonal cross section. Unlike in the Ni FNTs, the thermally evaporated Ni<sub>80</sub>Fe<sub>20</sub> shell was smooth and showed no discontinuities: its roughness was less than 5 nm. This improvement likely led to the observation of an idealized magnetization reversal behavior. Below a blocking temperature of 18 K and before field training, the DCM/nanoSQUID experiments also showed a pronounced exchange bias effect. In particular, the few-nanometer-thick native oxide on the Ni<sub>80</sub>Fe<sub>20</sub> FNTs pinned the magnetization, suppressing the nucleation of vortices at the FNT ends and the subsequent coherent magnetization reversal. These results highlighted the importance of either controlling the nature of the oxide capping layer in such FNTs or working well above the blocking temperature, where exchange bias is not effective (Fig. 17.7).

In 2016 and 2018, Gross et al. [66] performed DCM experiments on the CoFeB FNTs produced by magnetron sputtering and measured in MR by Rüffer et al. [58] and Baumgaertl et al. [59]. First, Gross et al. carried out measurements in three orientations of the applied field with respect to the FNTs, which were typically 10 μm long with 30-nm-thick and 250-nm-wide hexagonal shells. These FNTs were largely defect-free with a surface roughness better than 3 nm. Comparing measurements to an analytical model of an idealized Stoner-Wohlfarth magnet, the authors were able to model the system’s high-field behavior and extract each FNT’s saturation magnetization.

In addition, to model the DCM measurements at low field and to understand the magnetization configurations present near remanence, the authors developed a numerical simulation of the experiment using the Landau-Lifshitz-Gilbert micromagnetic formalism. For each value of  $H$ , the simulation determined the equilibrium magnetization configuration and the second derivative of  $E_m$  with respect to  $\theta_c$ , relating DCM signal to the magnetization configuration present in the FNT. These insights—combined with the high torque sensitivity provided by ultrasoft Si cantilevers—provided a detailed picture of the equilibrium magnetization configurations and reversal in the individual CoFeB FNTs.

The overall features of the DCM hysteresis loops measured by Gross et al. were consistent with the reversal sequences predicted by numerical simulations. Nevertheless, clear evidence for the presence of vortex configurations—in the form of prominent signature predicted by simulations to occur at the beginning of reversal upon vortex nucleation—was absent. Once again, experiments pointed to some discrepancy between the idealized model of FNT reversal and what happened in real samples. As in previous measurements the ends of the CoFeB FNTs measured by Gross et al. were not ideal. In particular, each FNT was terminated by a spherical CoFeB shell around a Ga droplet left over from the template GaAs NW growth. Furthermore, to mount the FNT onto a cantilever for DCM measurements, the other FNT end was broken off of the substrate. As a result, both ends of the FNTs were not capped by an open and perfectly flat end, as considered in theory.

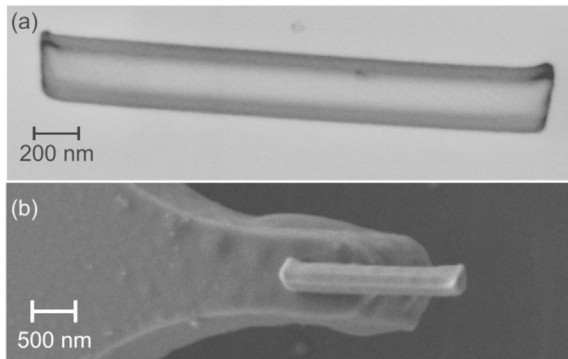


**Fig. 17.6** Scanning electron micrographs (SEMs) of the FIB milled 2.2- $\mu\text{m}$ -long FNT (A) placed on a Si surface and (B) attached to the tip of an ultrasoft Si cantilever.

Adapted from A. Mehl, B. Gross, M. Wyss, T. Schefer, G. Tütüncüoglu, F. Heimbach, A.F.i. Morral, D. Grundler, M. Poggio, Phys. Rev. B 97 (2018) 134422.

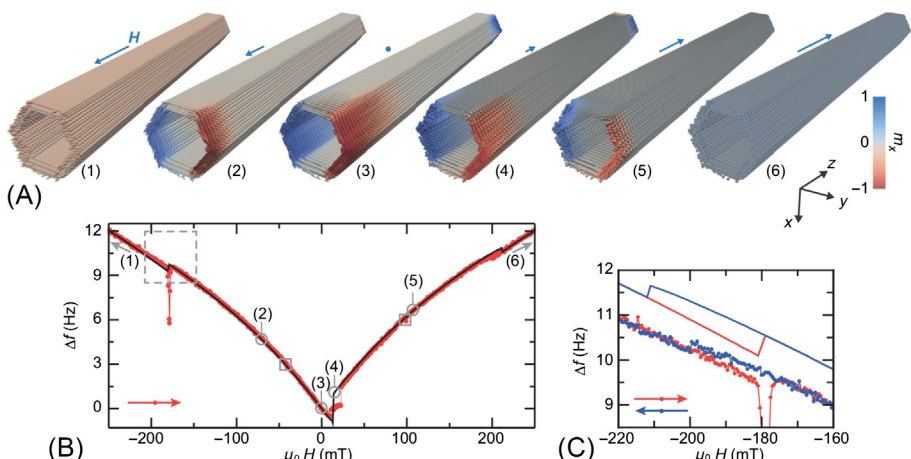


**Fig. 17.7** Simulated and measured reversal of a 2.2- $\mu\text{m}$ -long FNT. (A) Simulated magnetization configurations for  $\Delta f/H$  corresponding to the labels. (B) Simulated (lines) and measured (points) DCM signal. Squares highlight those simulated vortex domain nucleation/annihilation features, which are difficult to see. (C) A detailed view of DCM signature corresponding to the nucleation (annihilation) of the first vortex domain. The simulation, which is offset for clarity, uses  $\alpha_T = 6^\circ$ ,  $\alpha_B = 10.5^\circ$ , and  $\theta_H = 11.0^\circ$ . Adapted from A. Mehl, B. Gross, M. Wyss, T. Schefer, G. Tütüncüoglu, F. Heimbach, A.F.i. Morral, D. Grundler, M. Poggio, Phys. Rev. B 97 (2018) 134422.

To realize ideal ends and to study the dependence on the FNT length, in 2018, Mehl et al. studied CoFeB FNTs from the same sample set, whose ends had been cut using a focused ion beam (FIB) [77] (Fig. 17.6). This procedure ensured FNTs with smooth and well-defined ends, which—in general—were tilted relative to the plane normal to the FNT axis. This modification proved crucial and immediately resulted in clear experimental signatures of vortex end-domain nucleation in individual FNTs (Fig. 17.7). The correspondence between the measured and simulated DCM was such that the authors clearly confirmed that magnetization reversal was

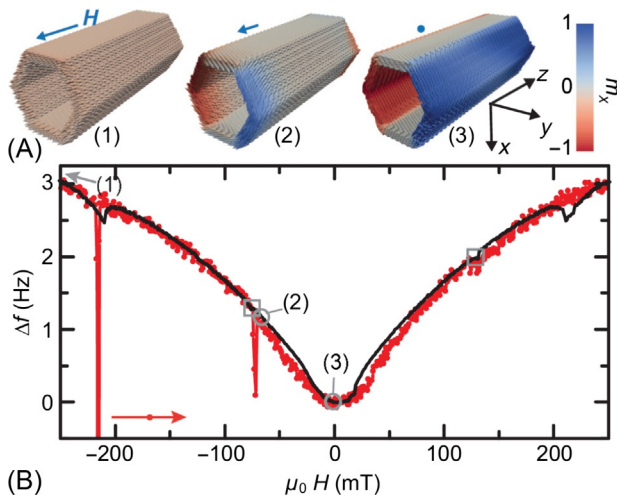


**Fig. 17.8** Simulated and measured reversal of a  $0.6\text{-}\mu\text{m}$ -long FNT. (A) Calculated magnetization configurations for  $\Delta f(H)$  corresponding to the labels. (B) Simulated (lines) and measured (points) DCM response. Squares highlight those simulated vortex nucleation/annihilation features, which are difficult to see. For the simulation,  $\alpha_T = 4.0^\circ$ ,  $\alpha_B = 6.5^\circ$ , and  $\theta_H = 10.0^\circ$ .

Adapted from A. Mehlin, B. Gross, M. Wyss, T. Schefer, G. Tütüncüoglu, F. Heimbach, A.F.i. Morral, D. Grundler, M. Poggio, Phys. Rev. B 97 (2018) 134422.

proceeding through vortex configurations. In addition, measurements of the shortest measured FNT, which was  $0.6\text{ }\mu\text{m}$  long, unambiguously indicated a reversal sequence that included a remanent global vortex state (Fig. 17.8). Finally, a study of the dependence of the end-vortex nucleation field on the angle of the FNTs ends showed that even slightly slanted ends can considerably shift the nucleation field. The close agreement between DCM measurements and simulations on the effect of slanted ends served as further confirmation that the simulated vortex nucleation process is an accurate description of what occurred in the measured samples. It also proved that FNTs fabricated from amorphous CoFeB with low surface roughness and FIB-defined ends were the experimental realization of the ideal FNTs discussed in the theoretical literature.

## 17.4 Magnetic imaging with X-rays

Magnetic imaging of ferromagnets with soft X-rays is carried out by measuring the difference in resonant absorption of  $\sigma^+$  and  $\sigma^-$  circularly polarized X-rays, due to X-ray magnetic circular dichroism (XMCD). This difference is proportional to the magnetic moment in the interaction volume projected along the beam propagation direction  $\hat{k}$ . Since the X-ray photon energy must be tuned in resonance with the absorption edge of a given element, the contrast is element specific and allows for

spectroscopic measurements of composition and oxidation states. Imaging is performed either by detecting transmitted X-ray photons, that is, transmission X-ray microscopy (TXM), or by collecting photoelectrons emitted from the sample upon absorption of the X-rays, that is, X-ray photoemission electron microscopy (XPEEM). These microscopies can have spatial resolutions down to 20 nm.

TXM can be carried out by focusing an X-ray beam on a sample and forming an image with the transmitted light. Alternatively, in scanning TXM (STXM), the focused beam can be scanned across the sample, while the total transmitted light is collected at each position. In either case, the sample thickness is limited to less than 200 nm and must be supported by a substrate, which is transparent to X-rays (e.g., SiN membrane).

In XPEEM, an image is formed by the secondary electrons excited by the X-ray beam illuminating the sample at grazing incidence (typically 16°). Therefore the XPEEM intensity at each position represents the local near-surface magnetization projected along  $\hat{k}$ . However, nonplanar structures, like the FNTs, also cast X-ray shadows on the supporting substrate. The XPEEM contrast from these regions depends on the integrated volume magnetization of the material, through which the X-rays have previously passed. Shadow XPEEM was pioneered by Kimling et al. [49] and further developed by Da Col et al. [21] and Jamet et al. [20] for FNWs.

In 2017, Wyss et al. [78] used shadow XPEEM to investigate the CoFeB and Ni<sub>80</sub>Fe<sub>20</sub> FNTs from the sample set first studied by Baumgaertl et al. [59] (Fig. 17.9). In the XPEEM experiments, which were carried out in remanence, the ends of the FNTs were cut flat using a FIB, just as was done later by Mehlin et al. [77]. The authors determined the remanent magnetization configuration of 19 CoFeB FNTs and 25 Ni<sub>80</sub>Fe<sub>20</sub> with a variety of lengths. The study revealed that short NTs can occupy a stable global vortex state in remanence. Consistent with an analytical theory by Landeros et al. [16] and numerical simulations carried out by the authors, the FNT length-to-diameter ratio was found to play a crucial role in stabilizing the global vortex state. XPEEM images of the equilibrium magnetization configurations showed that the relative circulation sense of vortex ends in real FNTs is less controlled than expected from idealized simulations. As a result, short FNTs were found not only in remnant global vortex states but also in opposing vortex states, which include a Néel wall between two opposing vortices. Additional simulations suggested that sample imperfections including variations in thickness and deviations from a perfect geometry were responsible for this discrepancy. Still, the XPEEM images of global vortex states showed that the most important properties predicted for idealized FNTs had been realized in real structures. They also demonstrated that the equilibrium magnetic configuration of a real FNT can be programmed via geometry, a result consistent with long-standing theoretical predictions.

Wyss et al. found that FNTs shorter than 2 μm with a diameter between 200 and 300 nm and a shell thickness of 30 nm occupied remanent vortex configurations (Fig. 17.11). As expected by calculations, longer FNTs occupied a remanent mixed-state configuration, in which the magnetization of the central part of the FNT aligns along its long axis and only curls into vortices at the ends [16, 29, 79] (Fig. 17.10). However, both for studies of spin-wave physics and for applications such as magnonic waveguides and data storage (e.g., racetrack memory) FNTs with large length-to-diameter ratios are required (Figs. 17.9–17.11).

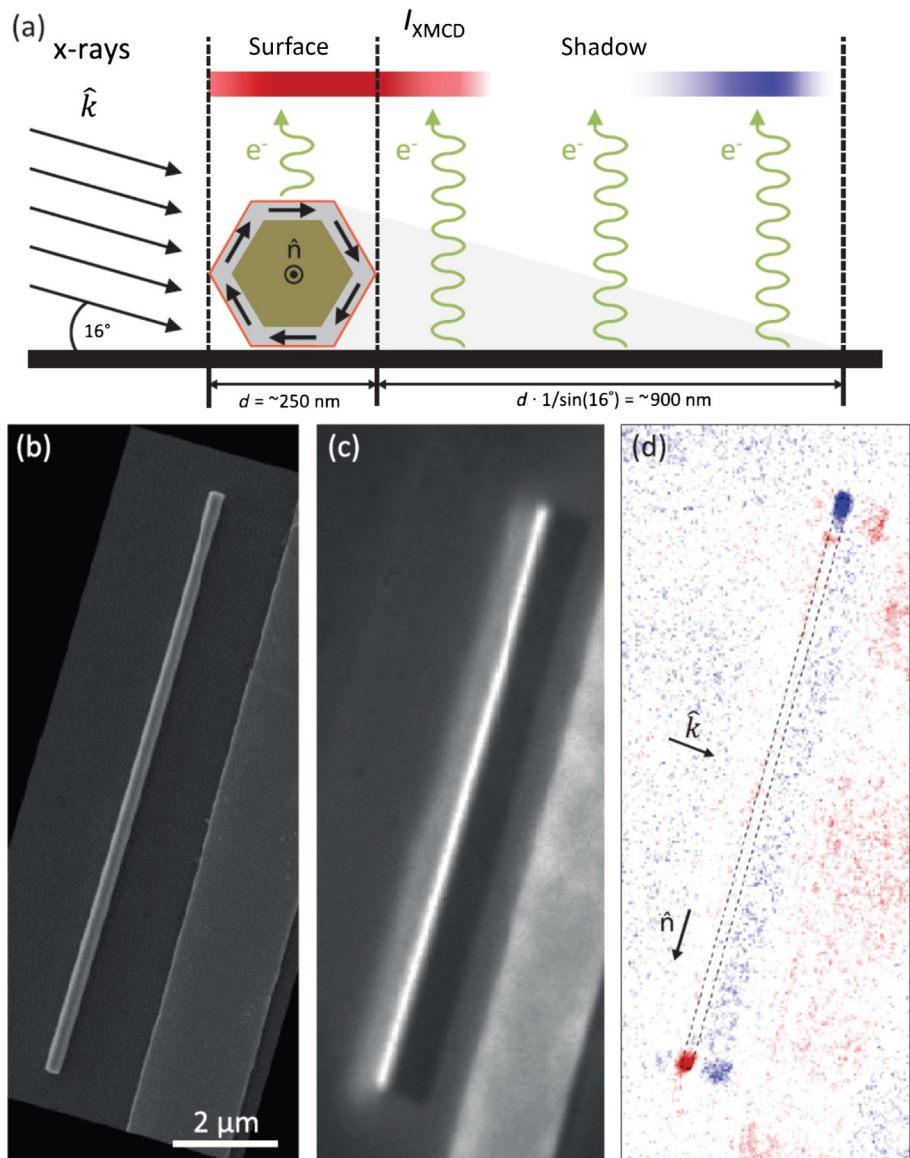


**Fig. 17.9** (A) Schematic drawing of a FNT cross section with incident X-rays, photoexcited electrons, and expected XPEEM contrast for the depicted vortex configuration. The brown central region depicts the nonmagnetic GaAs template material, the gray region the magnetic NT, and the red region the native oxide. (B) SEM of an 11.3- $\mu\text{m}$ -long CoFeB NT with a Au alignment marker visible on the right of the image. (C) PEEM image with gray-scale contrast corresponding to PEEM intensity and (D) XPEEM image with red (blue) contrast representing positive (negative) XMCD signal. The dashed line shows the position of the NT.  
Adapted from M. Wyss, A. Mehlin, B. Gross, A. Buchter, A. Farhan, M. Buzzi, A. Kleibert, G. Tütüncüoglu, F. Heimbach, A.F.i. Morral, D. Grundler, M. Poggio, Phys. Rev. B 96 (2017) 024423.

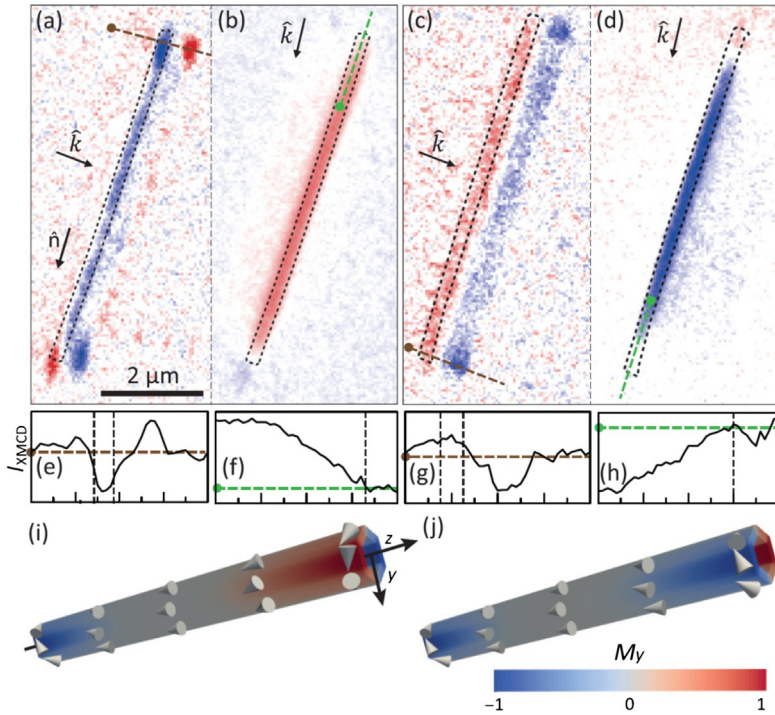


**Fig. 17.10** XPEEM images of a 6.9- $\mu\text{m}$ -long Py NT with (A)  $\hat{k} \perp \hat{n}$  and (B)  $\hat{k} \parallel \hat{n}$  and of a 7.2- $\mu\text{m}$ -long CoFeB NT with (C)  $\hat{k} \perp \hat{n}$  and (D)  $\hat{k} \parallel \hat{n}$ . Dashed outlines indicate the positions of the NTs. Panels (E–H) represent 2- $\mu\text{m}$ -long XMCD linecuts along the corresponding colored dashed lines in (A–D). In the linecuts the background intensity is indicated by the level of the horizontal dashed lines, and vertical dashed lines delineate the boundaries of the NT. Panels (I) and (J) show simulated remnant magnetic states for a NT with  $l = 2.1 \mu\text{m}$  and  $d = 245 \text{ nm}$ . Both configurations are mixed states with an axial central domain and vortex ends of either (I) opposing circulation—consistent with (A) and (B)—or (J) matching circulation, consistent with (C) and (D). The color scale corresponds to normalized magnetization along  $\hat{y}$ . Arrowheads indicate the local magnetization direction.

Adapted from M. Wyss, A. Mehlin, B. Gross, A. Buchter, A. Farhan, M. Buzzi, A. Kleibert, G. Tütüncüoglu, F. Heimbach, A.F.i. Morral, D. Grundler, M. Poggio, Phys. Rev. B 96 (2017) 024423.

To address this problem, in 2018, Stano et al. attempted to realize remanent vortex states in longer FNTs by exploiting magnetic anisotropy. The authors synthesized nanocrystalline CoNiB FNTs by electroless plating in porous templates with lengths up to 30  $\mu\text{m}$ , widths between 300 and 400 nm, and a shell thickness of 30 nm [80]. Magnetic imaging of individual specimens in remanence by both STXM and XPEEM revealed FNTs in purely azimuthal configurations, consisting of a series of well-defined vortex domains (Fig. 17.12). These configurations are stabilized by an effective anisotropy coefficient of the order of 10  $\text{kJ/m}^3$ , likely originating from a

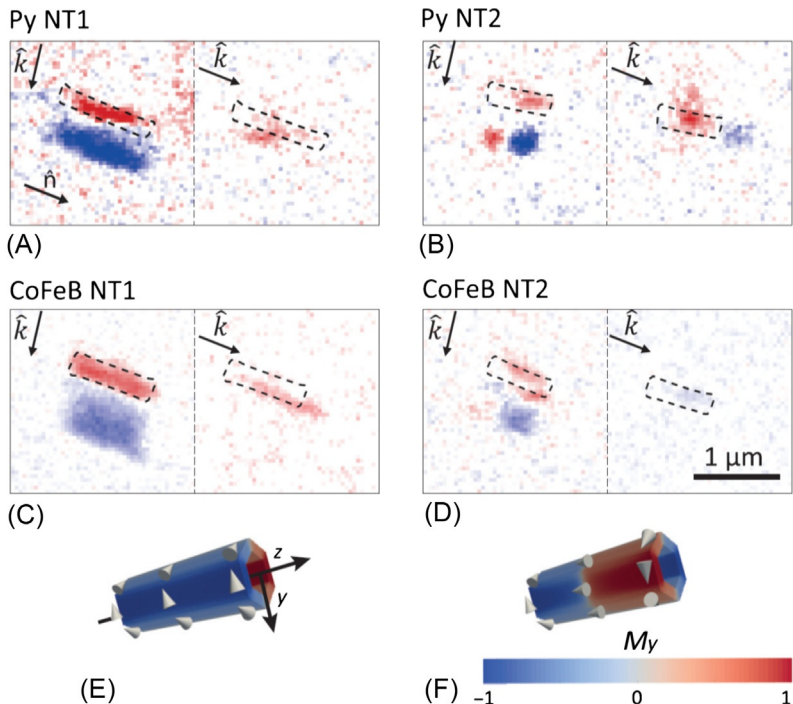


**Fig. 17.11** XPEEM images with  $\hat{k} \perp \hat{n}$  and  $\hat{k} \parallel \hat{n}$  of short NTs. (A) 1.3- $\mu\text{m}$ -long Py FNT found in a global vortex state. (B) 0.73- $\mu\text{m}$ -long Py FNT in an opposing vortex state. (C) 1.06- $\mu\text{m}$ -long CoFeB NT in a global vortex state. (D) 0.83- $\mu\text{m}$ -long CoFeB NT in an opposing vortex state. Simulated equilibrium states of FNTs ( $l = 610$  nm,  $d = 245$  nm) in (E) a global vortex state and in (F) an opposing vortex state. The color scale corresponds to the normalized magnetization along  $\hat{y}$ . Arrowheads indicate the local magnetization direction.

Adapted from M. Wyss, A. Mehl, B. Gross, A. Buchter, A. Farhan, M. Buzzi, A. Kleibert, G. Tütüncüoglu, F. Heimbach, A.F.i. Morral, D. Grundler, M. Poggio, Phys. Rev. B 96 (2017) 024423.

magnetoelastic coupling and/or anisotropic interfacial magnetic anisotropy. This result means that the strength of this anisotropy and thus the type of remanent magnetic configuration (axial or azimuthal domains) can be tailored through annealing or material composition.

Similar results were reported in 2018 by Zimmermann et al., who combined MR and STXM to investigate the remanent configurations in  $\text{Ni}_{80}\text{Fe}_{20}$  FNTs with lengths from 10 to 30  $\mu\text{m}$ , a width of 500 nm, and a shell thickness of 30 nm [61]. They found stable azimuthal configurations, consisting of vortex domains, independent of the length of the FNTs, again pointing to a stabilizing anisotropy. Analysis of the MR data and comparison with micromagnetic simulations allowed the determination of the strength of the magnetic anisotropy for individual FNTs. Using an  $\text{Al}_2\text{O}_3$  buffer layer between the  $\text{Ni}_{80}\text{Fe}_{20}$  shell and the template GaAs NW, the

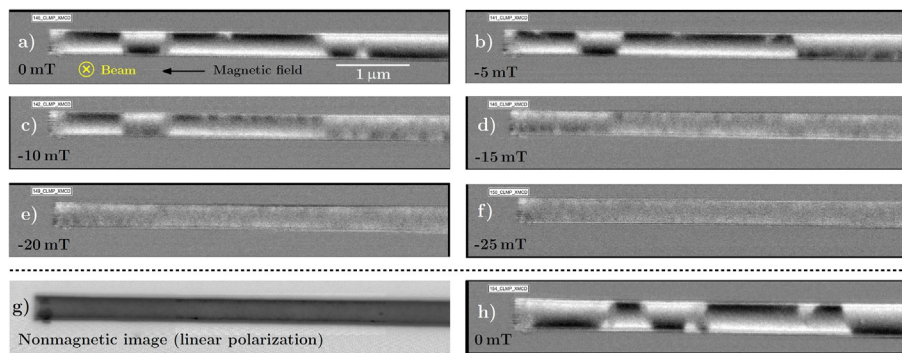


**Fig. 17.12** STXM under external magnetic field-anisotropy strength determination. (A–F) XMCD magnetic images (Co-L3 edge, same contrast range 15%) under axial magnetic field. With increasing field magnitude, the STXM contrast vanishes, showing that magnetization rotates toward the axial direction. Around 25 mT is needed for the saturation of tubes along the axial direction. Field of view (A–G)  $6.0 \times 1.0 \mu\text{m}^2$  and (H)  $4.8 \times 0.8 \mu\text{m}^2$ . (G) Nonmagnetic STXM image (linear polarization of X-rays) highlighting the tubular structure. (H) XMCD image after removing magnetic field (after sequence A–F). Even at zero field the transition between neighboring domains is not as sharp as in XMCD-PEEM images; this we attribute to sample ageing (STXM done 1 year after XPEEM).

Adapted from M. Staňo, S. Schaefer, A. Wartelle, M. Rioult, R. Belkhoud, A. Sala, T. O. Menteş, A. Locatelli, L. Cagnon, B. Trapp, S. Bochmann, S. Martin, E. Gautier, J.-C. Toussaint, W. Ensinger, O. Fruchart, Sci. Post Phys. 5 (2018) 038.

anisotropy could be tuned such that the vortex configuration was less stable to externally applied magnetic fields. The authors ultimately concluded that the observed vortex configurations are favored by a tunable growth-induced azimuthal anisotropy, which, in turn, can be understood as a result of a shadowing effect occurring during growth at oblique angles (Fig. 17.13). Furthermore, the authors showed that stable vortex domains can be introduced by external magnetic fields and can be erased by radio-frequency magnetic fields applied at the center of the tubes via a strip line antenna (Fig. 17.14).

## 17.5 Scanning SQUID microscopy

Scanning SQUID microscopy is an extremely sensitive method for spatially mapping the stray magnetic field due to a magnetic sample. Typically, it relies on a scanning SQUID or pick-up loop with diameter larger than several micrometers. The size of the scanning sensor, along with its minimal distance from the sample, limits the attainable spatial resolution. Although nanoSQUIDs have been used to detect the stray field due to the end of an FNT [74–76], their geometry makes full scanning probe imaging awkward, because they are usually fabricated by lithographic methods in the middle of a planar substrate. Recently, however, researchers have succeeded in producing so-called SQUID-on-tip (SOT) sensors, which allow for nanometer-scale imaging resolution with demonstrated field sensitivities down to  $5 \text{ nT}/\text{Hz}^{1/2}$  [81,82]. These

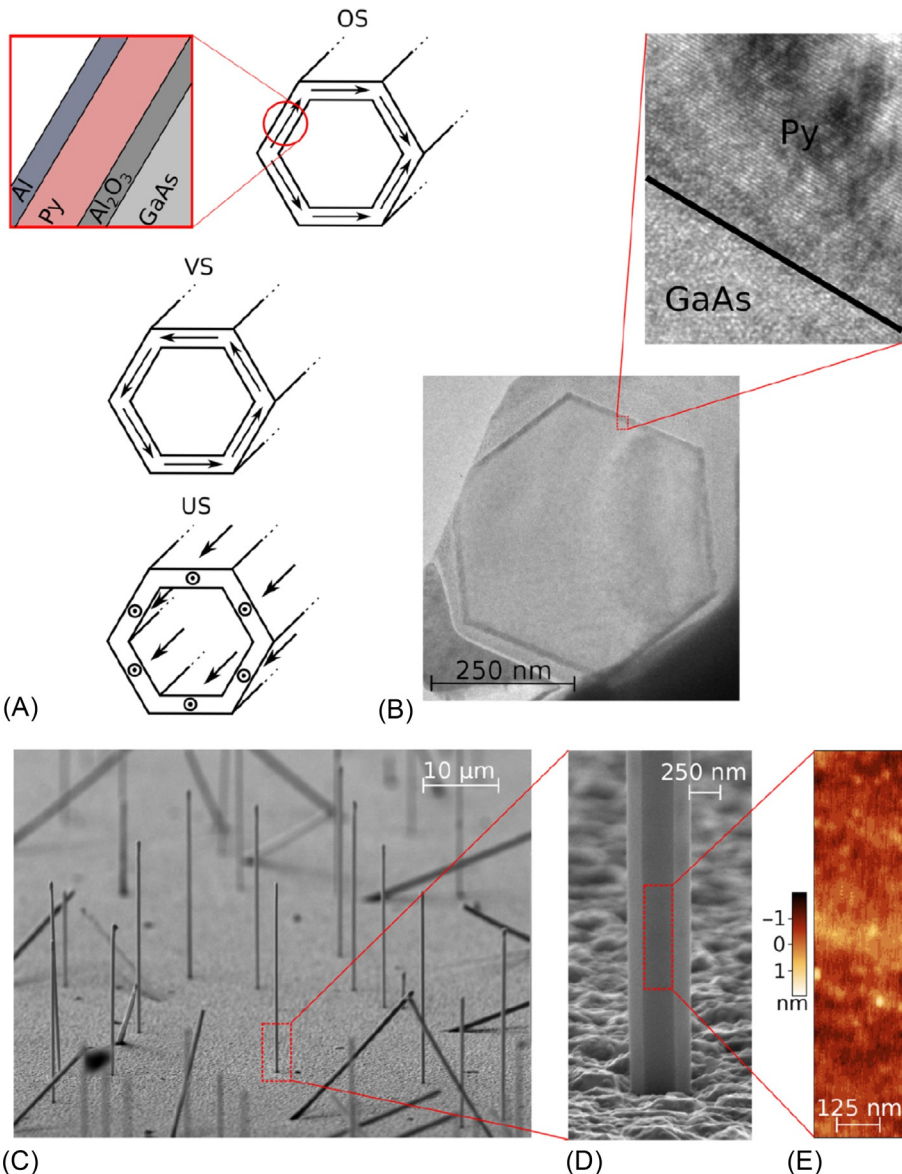


**Fig. 17.13** Illustration of different states found in FNTs and sketch of the layers deposited on the GaAs core. (A) While the vortex state (VS) and the uniform state (US) may appear as magnetic ground states, the onion state (OS) is metastable and can only be entered after the application of an external magnetic field. (B) Cross-sectional TEM image of sample s1. The inset shows an enlargement of the border between GaAs and Py. The crystalline structure of Py can be identified. (C) SEM image of the free-standing, low-density NTs that are individually selected for the experiments. (D) Hexagonally shaped NTs exhibiting a very smooth surface after metal-layer deposition. (E) AFM images of the facets reveals a root-mean-squared roughness of  $R_{\text{rms}} = 0.4 \text{ nm}$ .

Adapted from M. Zimmermann, T.N.G. Meier, F. Dirnberger, A. Kákay, M. Decker, S. Wintz, S. Finizio, E. Josten, J. Raabe, M. Kronseder, D. Bougeard, J. Lindner, C.H. Back, Nano Lett. 18 (2018) 2828–2834.

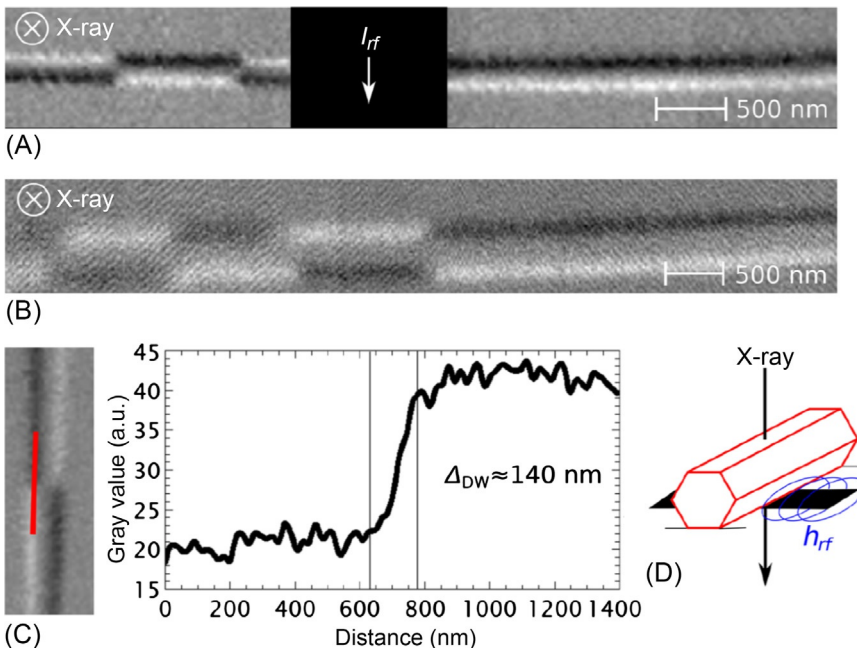


**Fig. 17.14** XMCD images obtained with STXM at zero applied magnetic field. Black-and-white contrast corresponds to a magnetization component pointing parallel and antiparallel to the X-ray beam direction, which is illustrated in panel D. (A) A 210-nm-diameter tube placed on top of a 1- $\mu\text{m}$ -wide antenna to be able to apply rf-excitation fields. (B) A 500-nm-diameter tube. Domains are clearly visible for both tube types. (C) An enlarged image section of the 210-nm tube. A line scan is shown along the red line to estimate an upper bound of the domain wall width of 140 nm. The lateral size of the X-ray beam is approximately 40 nm. (D) Illustration of the X-ray beam direction with respect to the NT facet orientation. The excitation rf field is generated by the strip antenna.

Adapted from M. Zimmermann, T.N.G. Meier, F. Dirnberger, A. Kákay, M. Decker, S. Wintz, S. Finizio, E. Josten, J. Raabe, M. Kronseder, D. Bougeard, J. Lindner, C.H. Back, *Nano Lett.* 18 (2018) 2828–2834.

devices consist of a SQUID fabricated by thermal evaporation on the end of a pulled quartz capillary. This long and thin device acts as a natural scanning probe that measures the magnetic flux threading through its loop diameter, which can be as small as 50 nm.

In 2018, Vasyukov et al. [83] used a scanning SOT to map the stray magnetic field produced by individual CoFeB FNTs from the sample set first studied by Baumgaertl et al. [59] (Fig. 17.15). Images were taken as a function of applied magnetic field as each FNT was led through magnetic reversal and were compared with micromagnetic simulations (Fig. 17.16). In magnetic fields applied perpendicular to the FNT long axis, their magnetization appears to reverse through vortex states, that is, configurations with vortex end domains or in the case of a sufficiently short FNT with a single global vortex. Geometrical imperfections in the samples and the resulting distortion of

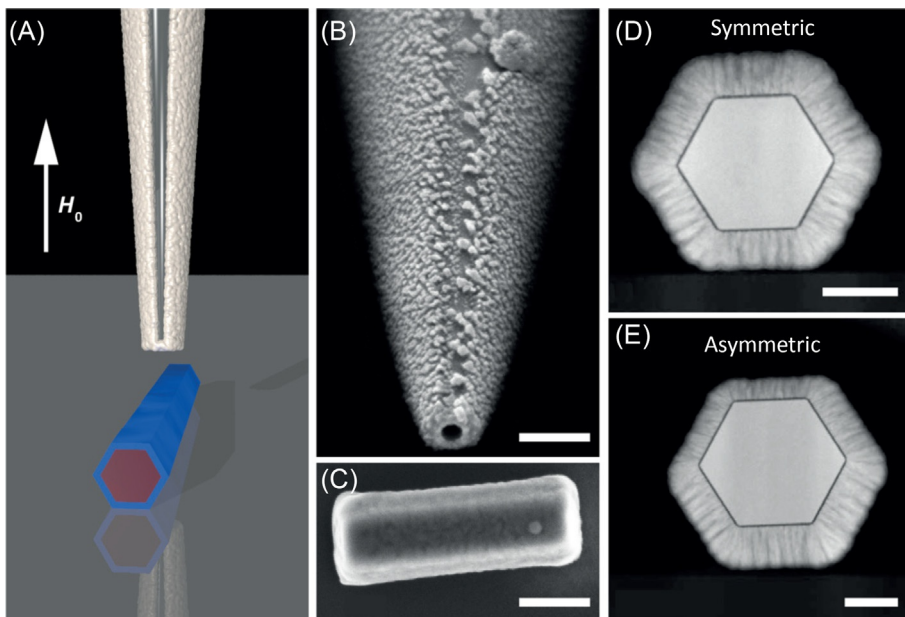


**Fig. 17.15** Experimental setup. (A) Schematic drawing showing the scanning SOT, a FNT lying on the substrate, and the direction of  $H_0$ . The CoFeB shell is depicted in blue and the GaAs core in red. Pb on the SOT is shown in white. SEMs of the (B) the SOT tip and (C) a 0.7- $\mu\text{m}$ -long FNT. (D and E) Cross-sectional HAADF STEMs of two FNTs from a similar growth batch as those measured. The scale bars represent 200 nm (B and C) and 50 nm in (D and E).

Adapted from D. Vasyukov, L. Ceccarelli, M. Wyss, B. Gross, A. Schwab, A. Mehlin, N. Rossi, G. Tütüncüoglu, F. Heimbach, R.R. Zamani, A. Kovács, A.F.i. Morral, D. Grundler, M. Poggio, *Nano Lett.* 18 (2018) 964.

idealized magnetization configurations influenced the measured stray-field patterns. The authors found that finer control of the sample geometry is required to reduce these distortions and for such devices to be considered as elements in ultrahigh-density magnetic storage. Nevertheless, the remanent global vortex state was shown to be robust to the imperfections of real samples: despite slight distortions, it continues to be dominated by a single azimuthally aligned vortex.

## 17.6 Magnetic force microscopy

Among the most successful tools for nanometer-scale magnetic imaging is MFM. It was introduced in the late 1980s as a natural extension of atomic force microscopy. These days, it is performed in air, liquid, and vacuum and at a variety of temperatures. Under ideal conditions, state-of-the-art MFM can reach spatial resolutions down to 10 nm [84], though more typically around 100 nm.

The first MFM images of individual FNTs were reported in 2008 by Li et al. [85]. They prepared arrays of single-crystal Co FNTs by electroplating. SQUID

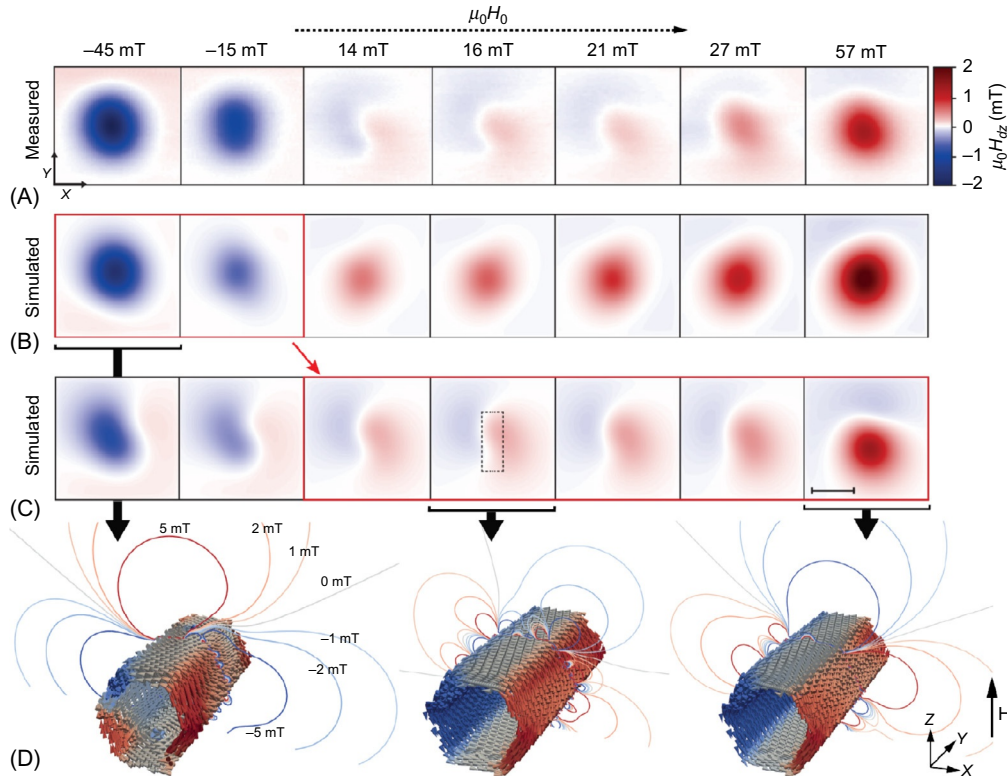


**Fig. 17.16** Magnetic reversal of a  $0.7\text{-}\mu\text{m}$ -long FNT ( $l = 0.69 \mu\text{m}$ ,  $d = 250 \text{ nm}$ ) in a field applied perpendicular to its long axis. Images of the stray-field component along  $\hat{z}$ ,  $H_{dz}$ , in the  $xy$ -plane  $300 \text{ nm}$  above the FNT for the labeled values of  $H_0$  (A) as measured by the scanning SOT. (B and C) Numerical simulations of  $H_{dz}$  produced by two progressions of equilibrium magnetization configurations with different initial conditions. The dashed line delineates the position of the FNT, and the scale bar corresponds to  $0.5 \mu\text{m}$ . (D) Magnetization configurations and contours of constant  $H_{dz}$  corresponding to three values of  $H_0$ . The configuration on the left is characterized by two vortices in the top and bottom facets, respectively. The middle and right configurations are distorted global vortex states. Arrows indicate the direction of the magnetization, while red (blue) contrast corresponds to the magnetization component along  $\hat{z}$  ( $-\hat{z}$ ).

Adapted from D. Vasyukov, L. Ceccarelli, M. Wyss, B. Gross, A. Schwab, A. Mehlin, N. Rossi, G. Tütüncüoglu, F. Heimbach, R.R. Zamani, A. Kovács, A.F.i. Morral, D. Grundler, M. Poggio, Nano Lett. 18 (2018) 964.

magnetometry and selective area electron diffraction measurements on the array of FNTs lead the authors to conclude that their FNTs occupied vortex-like flux-closure configurations in remanence. This conclusion was supported by the presence of a magnetocrystalline anisotropy perpendicular to the FNT long axis in these samples. They also interpreted the weak MFM contrast produced by an individual FNT as further evidence of a remanent global vortex state, whose flux-closure configuration should produce no stray field.

As shown later by Staňo [86], the weak MFM signal produced by the FNT was likely due to the difficulty in achieving pure magnetic contrast. Under typical conditions—especially for nonplanar samples such as FNTs—spurious topographic or electrostatic contrast can be misinterpreted as magnetic signal. Note that X-ray microscopies and scanning SQUID do not suffer from this limitation. In his later work, Staňo also imaged individual FNTs by MFM. He studied the same CoNiB FNTs imaged by himself and coauthors using STXM and XPEEM. His MFM images confirmed the presence of stable remanent azimuthal configurations, consisting of vortex domains, independent of the length of the FNTs.

## 17.7 Conclusions and outlook

As discussed in this chapter, a number of techniques capable of measuring individual FNTs have emerged in the last decade. The resulting measurements have been crucial in clarifying how close real FNTs are to exhibiting the magnetic properties predicted by theory. In particular, early MR and DCM measurements were not fully consistent with theoretical predictions, suggesting that the roughness and ill-defined ends of real FNTs were playing an important role. This hypothesis was later confirmed in follow-up DCM, XPEEM, and SOT experiments, which showed a nearly ideal magnetic behavior, once roughness was reduced and the FNT ends were properly defined. Nevertheless, these measurements also showed the role of residual defects and imperfections in distorting the equilibrium magnetization configurations predicted by theory and—in some cases—in stabilizing configurations that were not predicted. Most recent experiments on single FNTs including STXM, XPEEM, and MR have shown how interfacial anisotropy, which can be controlled during growth, can help to stabilize vortex-like flux-closure configurations. This stabilization mechanism can be exploited to counteract the destabilizing effect of sample imperfections and, ultimately, to make devices with a robust and reproducible magnetic behavior.

It is now clear that the push by several research groups to measure the magnetic behavior of individual FNTs has had a strong impact on our understanding of how best to fabricate FNTs and how to adjust theory to better reflect the behavior of real devices. Many of these insights would not have been possible without single-specimen sensitivity, that is, using only magnetization measurements of large arrays. Nevertheless, much work remains before FNTs can be integrated into three-dimensional memory devices or used in magnonic devices. For example, further measurements should be carried out to understand the role of defects in FNTs and how they lead to magnetic pinning. This may require the application of magnetic imaging techniques with improved spatial resolution compared with what has been used until now. Imaging

experiments combining both high spatial resolution and large frequency bandwidth will also be crucial for investigating domain wall motion and the propagation of spin waves in FNTs.

Given that the first steps toward measuring single FNTs have now been taken using a wide variety of techniques, it is likely that the next stage of experimental development will bring a number of improvements in the application of each technique. These improved measurements will undoubtedly lead to new physical insights into these fascinating and potentially useful magnetic nanostructures.

## References

- [1] R.P. Cowburn, M.E. Welland, Room temperature magnetic quantum cellular automata, *Science* 287 (2000) 1466–1468.
- [2] M.M. Maqableh, X. Huang, S.-Y. Sung, K.S.M. Reddy, G. Norby, R.H. Victora, B.J.H. Stadler, Low-resistivity 10 nm diameter magnetic sensors, *Nano Lett.* 12 (2012) 4102–4109.
- [3] S. Khizroev, M.H. Kryder, D. Litvinov, D.A. Thompson, Direct observation of magnetization switching in focused-ion-beam-fabricated magnetic nanotubes, *Appl. Phys. Lett.* 81 (2002) 2256–2257.
- [4] M. Poggio, C.L. Degen, Force-detected nuclear magnetic resonance: recent advances and future challenges, *Nanotechnology* 21 (2010) 342001.
- [5] H. Campanella, M. Jaafar, J. Llobet, J. Esteve, M. Vázquez, A. Asenjo, R.P. del Real, J.A. Plaza, Nanomagnets with high shape anisotropy and strong crystalline anisotropy: perspectives on magnetic force microscopy, *Nanotechnology* 22 (2011) 505301.
- [6] Y. Zheng, J.-G. Zhu, Switching field variation in patterned submicron magnetic film elements, *J. Appl. Phys.* 81 (1997) 5471–5473.
- [7] O. Fruchart, J.-P. Nozières, W. Wernsdorfer, D. Givord, F. Rousseaux, D. Decanini, Enhanced coercivity in submicrometer-sized ultrathin epitaxial dots with in-plane magnetization, *Phys. Rev. Lett.* 82 (1999) 1305–1308.
- [8] J.M.D. Coey, *Magnetism and Magnetic Materials*, Cambridge University Press, Cambridge, UK, 2010.
- [9] T.R. Koehler, D.R. Fredkin, Micromagnetic modeling of permalloy particles: thickness effects, *IEEE Trans. Magn.* 27 (1991) 4763–4765.
- [10] T. Schrefl, J. Fidler, K.J. Kirk, J.N. Chapman, Domain structures and switching mechanisms in patterned magnetic elements, *J. Magn. Magn. Mater.* 175 (1997) 193–204.
- [11] J. Rothman, M. Kläui, L. Lopez-Diaz, C.A.F. Vaz, A. Bleloch, J.A.C. Bland, Z. Cui, R. Speaks, Observation of a bi-domain state and nucleation free switching in mesoscopic ring magnets, *Phys. Rev. Lett.* 86 (2001) 1098–1101.
- [12] B. Hausmanns, T.P. Krome, G. Dumpich, E.F. Wassermann, D. Hinzke, U. Nowak, K.D. Usadel, Magnetization reversal process in thin Co nanowires, *J. Magn. Magn. Mater.* 240 (2002) 297–300.
- [13] A.D. Kent, D.L. Stein, Annular spin-transfer memory element, *IEEE Trans. Nanotechnol.* 10 (2011) 129–134.
- [14] X.F. Han, Z.C. Wen, H.X. Wei, Nanoring magnetic tunnel junction and its application in magnetic random access memory demo devices with spin-polarized current switching (invited), *J. Appl. Phys.* 103 (2008) 07E933.
- [15] L. Lopez-Diaz, J. Rothman, M. Kläui, J.A.C. Bland, Computational study of first magnetization curves in small rings, *IEEE Trans. Magn.* 36 (2000) 3155–3157.

- [16] P. Landeros, O.J. Suarez, A. Cuchillo, P. Vargas, Equilibrium states and vortex domain wall nucleation in ferromagnetic nanotubes, *Phys. Rev. B* 79 (2009) 024404.
- [17] K. Sattler, *Handbook of Nanophysics: Nanotubes and Nanowires*, CRC Press, Boca Raton, 2010. Available at: <https://www.crcpress.com/Handbook-of-Nanophysics-Nanotubes-and-Nanowires/Sattler/p/book/9781420075427> Accessed 20 February 2019.
- [18] C.T. Sousa, D.C. Leitao, M.P. Proenca, J. Ventura, A.M. Pereira, J.P. Araujo, Nanoporous alumina as templates for multifunctional applications, *Appl. Phys. Rev.* 1 (2014) 031102.
- [19] E. Brück, *Handbook of Magnetic Materials*, vol. 27, first ed., Elsevier, Amsterdam, 2018. Available at: <https://www.elsevier.com/books/handbook-of-magnetic-materials;bruck/978-0-444-64161-8> Accessed 20 February 2019.
- [20] S. Jamet, S. Da Col, N. Rougemaille, A. Wartelle, A. Locatelli, T.O. Menteş, B. Santos Burgos, R. Afid, L. Cagnon, S. Bochmann, J. Bachmann, O. Fruchart, J.C. Toussaint, Quantitative analysis of shadow x-ray magnetic circular dichroism photoemission electron microscopy, *Phys. Rev. B* 92 (2015) 144428.
- [21] S. Da Col, S. Jamet, N. Rougemaille, A. Locatelli, T.O. Mentes, B.S. Burgos, R. Afid, M. Darques, L. Cagnon, J.C. Toussaint, O. Fruchart, Observation of Bloch-point domain walls in cylindrical magnetic nanowires, *Phys. Rev. B* 89 (2014) 180405.
- [22] N.A. Usov, A. Zhukov, J. Gonzalez, Domain walls and magnetization reversal process in soft magnetic nanowires and nanotubes, *J. Magn. Magn. Mater.* 316 (2007) 255–261.
- [23] P. Landeros, S. Allende, J. Escrig, E. Salcedo, D. Altbir, E.E. Vogel, Reversal modes in magnetic nanotubes, *Appl. Phys. Lett.* 90 (2007) 102501.
- [24] Y. Gaididei, V.P. Kravchuk, D.D. Sheka, Curvature effects in thin magnetic shells, *Phys. Rev. Lett.* 112 (2014) 257203.
- [25] R. Streubel, P. Fischer, F. Kronast, V.P. Kravchuk, D.D. Sheka, Y. Gaididei, O.G. Schmidt, D. Makarov, Magnetism in curved geometries, *J. Phys. D. Appl. Phys.* 49 (2016) 363001.
- [26] J.A. Otálora, M. Yan, H. Schultheiss, R. Hertel, A. Kákay, Curvature-induced asymmetric spin-wave dispersion, *Phys. Rev. Lett.* 117 (2016) 227203.
- [27] M. Yan, A. Kákay, C. Andreas, R. Hertel, Spin-Cherenkov effect and magnonic Mach cones, *Phys. Rev. B* 88 (2013) 220412.
- [28] A.-P. Chen, J.M. Gonzalez, K.Y. Guslienko, Magnetization configurations and reversal of magnetic nanotubes with opposite chiralities of the end domains, *J. Appl. Phys.* 109 (2011) 073923.
- [29] A.P. Chen, N.A. Usov, J.M. Blanco, J. Gonzalez, Equilibrium magnetization states in magnetic nanotubes and their evolution in external magnetic field, *J. Magn. Magn. Mater.* 316 (2007) e317–e319.
- [30] A.P. Chen, K.Y. Guslienko, J. Gonzalez, Magnetization configurations and reversal of thin magnetic nanotubes with uniaxial anisotropy, *J. Appl. Phys.* 108 (2010) 083920.
- [31] J. Escrig, J. Bachmann, J. Jing, M. Daub, D. Altbir, K. Nielsch, Crossover between two different magnetization reversal modes in arrays of iron oxide nanotubes, *Phys. Rev. B* 77 (2008) 214421.
- [32] J. Bachmann, J. Escrig, K. Pitzschel, J.M.M. Moreno, J. Jing, D. Görlitz, D. Altbir, K. Nielsch, Size effects in ordered arrays of magnetic nanotubes: pick your reversal mode, *J. Appl. Phys.* 105 (2009) 07B521.
- [33] O. Albrecht, R. Zierold, S. Allende, J. Escrig, C. Patzig, B. Rauschenbach, K. Nielsch, D. Görlitz, Experimental evidence for an angular dependent transition of magnetization reversal modes in magnetic nanotubes, *J. Appl. Phys.* 109 (2011) 093910.
- [34] J. Bachmann, M. Jing, S. Knez, H. Barth, S. Shen, U.G. Mathur, K. Nielsch, Ordered iron oxide nanotube arrays of controlled geometry and tunable magnetism by atomic layer deposition, *J. Am. Chem. Soc.* 129 (2007) 9554–9555.

- [35] M. Daub, M. Knez, U. Goesele, K. Nielsch, Ferromagnetic nanotubes by atomic layer deposition in anodic alumina membranes, *J. Appl. Phys.* 101 (2007) 09J111.
- [36] A. Rudolph, M. Soda, M. Kiessling, T. Wojtowicz, D. Schuh, W. Wegscheider, J. Zweck, C. Back, E. Reiger, Ferromagnetic GaAs/GaMnAs core-shell nanowires grown by molecular beam epitaxy, *Nano Lett.* 9 (2009) 3860–3866.
- [37] Y.T. Chong, D. Görlitz, S. Martens, M.Y.E. Yau, S. Allende, J. Bachmann, K. Nielsch, Multilayered core/shell nanowires displaying two distinct magnetic switching events, *Adv. Mater.* 22 (2010) 2435–2439.
- [38] J. Escrig, S. Allende, D. Altbir, M. Bahiana, Magnetostatic interactions between magnetic nanotubes, *Appl. Phys. Lett.* 93 (2008) 023101.
- [39] W. Wernsdorfer, B. Doudin, D. Mailly, K. Hasselbach, A. Benoit, J. Meier, J.-P. Ansermet, B. Barbara, Nucleation of magnetization reversal in individual nanosized nickel wires, *Phys. Rev. Lett.* 77 (1996) 1873–1876.
- [40] R. Hertel, J. Kirschner, Magnetic drops in a soft-magnetic cylinder, *J. Magn. Magn. Mater.* 278 (2004) L291–L297.
- [41] C. Beeli, B. Doudin, J.-P. Ansermet, P.A. Stadelmann, Measurement of the remanent magnetization of single Co/Cu and Ni nanowires by off-axis TEM electron holography, *Ultramicroscopy* 67 (1997) 143–151.
- [42] L. Belliard, J. Miltat, A. Thiaville, S. Dubois, J.L. Duvail, L. Piraud, Observing magnetic nanowires by means of magnetic force microscopy, *J. Magn. Magn. Mater.* 190 (1998) 1–16.
- [43] Y. Henry, K. Ounadjela, L. Piraud, S. Dubois, J.-M. George, J.-L. Duvail, Magnetic anisotropy and domain patterns in electrodeposited cobalt nanowires, *Eur. Phys. J. B* 20 (2001) 35–54.
- [44] J. Wegrowe, S.E. Gilbert, D. Kelly, B. Doudin, J. Ansermet, Anisotropic magnetoresistance as a probe of magnetization reversal in individual nano-sized nickel wires, *IEEE Trans. Magn.* 34 (1998) 903–905.
- [45] J.-E. Wegrowe, D. Kelly, A. Franck, S.E. Gilbert, J.-P. Ansermet, Magnetoresistance of ferromagnetic nanowires, *Phys. Rev. Lett.* 82 (1999) 3681–3684.
- [46] S. Pignard, G. Goglio, A. Radulescu, L. Piraud, S. Dubois, A. Declémé, J.L. Duvail, Study of the magnetization reversal in individual nickel nanowires, *J. Appl. Phys.* 87 (1999) 824–829.
- [47] U. Ebels, A. Radulescu, Y. Henry, L. Piraud, K. Ounadjela, Spin accumulation and domain wall magnetoresistance in 35 nm Co wires, *Phys. Rev. Lett.* 84 (2000) 983–986.
- [48] L. Vila, L. Piraud, J.M. George, G. Faini, Multiprobe magnetoresistance measurements on isolated magnetic nanowires, *Appl. Phys. Lett.* 80 (2002) 3805–3807.
- [49] J. Kimling, F. Kronast, S. Martens, T. Böhnert, M. Martens, J. Herrero-Albillos, L. Tatibismaths, U. Merkt, K. Nielsch, G. Meier, Photoemission electron microscopy of three-dimensional magnetization configurations in core-shell nanostructures, *Phys. Rev. B* 84 (2011) 174406.
- [50] R. Streubel, J. Lee, D. Makarov, M.-Y. Im, D. Karnaushenko, L. Han, R. Schäfer, P. Fischer, S.-K. Kim, O.G. Schmidt, Magnetic microstructure of rolled-up single-layer ferromagnetic nanomembranes, *Adv. Mater.* 26 (2014) 316–323.
- [51] R. Streubel, D.J. Thurmer, D. Makarov, F. Kronast, T. Kosub, V. Kravchuk, D.D. Sheka, Y. Gaididei, R. Schäfer, O.G. Schmidt, Magnetically capped rolled-up nanomembranes, *Nano Lett.* 12 (2012) 3961–3966.
- [52] R. Streubel, F. Kronast, P. Fischer, D. Parkinson, O.G. Schmidt, D. Makarov, Retrieving spin textures on curved magnetic thin films with full-field soft X-ray microscopies, *Nat. Commun.* 6 (2015) 7612.

- [53] R. Streubel, L. Han, F. Kronast, A.A. Ünal, O.G. Schmidt, D. Makarov, Imaging of buried 3D magnetic rolled-up nanomembranes, *Nano Lett.* 14 (2014) 3981–3986.
- [54] D. Zhang, Z. Liu, S. Han, C. Li, B. Lei, M.P. Stewart, J.M. Tour, C. Zhou, Magnetite ( $\text{Fe}_3\text{O}_4$ ) core–shell nanowires: synthesis and magnetoresistance, *Nano Lett.* 4 (2004) 2151–2155.
- [55] J. Liang, J. Wang, A. Paul, B.J. Cooley, D.W. Rench, N.S. Dellas, S.E. Mohney, R. Engel-Herbert, N. Samarth, Measurement and simulation of anisotropic magnetoresistance in single GaAs/MnAs core/shell nanowires, *Appl. Phys. Lett.* 100 (2012) 182402.
- [56] C. Butschkow, E. Reiger, A. Rudolph, S. Geißler, D. Neumaier, M. Soda, D. Schuh, G. Woltersdorf, W. Wegscheider, D. Weiss, Origin of negative magnetoresistance of GaAs/(Ga,Mn)As core-shell nanowires, *Phys. Rev. B* 87 (2013) 245303.
- [57] D. Rüffer, R. Huber, P. Berberich, S. Albert, E. Russo-Averchi, M. Heiss, J. Arbiol, A.F.i. Morral, D. Grundler, Magnetic states of an individual Ni nanotube probed by anisotropic magnetoresistance, *Nanoscale* 4 (2012) 4989–4995.
- [58] D. Rüffer, M. Slot, R. Huber, T. Schwarze, F. Heimbach, G. Tütüncüoglu, F. Matteini, E. Russo-Averchi, A. Kovács, R. Dunin-Borkowski, R.R. Zamani, J.R. Morante, J. Arbiol, A.F.i. Morral, D. Grundler, Anisotropic magnetoresistance of individual CoFeB and Ni nanotubes with values of up to 1.4% at room temperature, *APL Mater.* 2 (2014) 076112.
- [59] K. Baumgaertl, F. Heimbach, S. Maendl, D. Rueffer, A.F.i. Morral, D. Grundler, Magnetization reversal in individual Py and CoFeB nanotubes locally probed via anisotropic magnetoresistance and anomalous Nernst effect, *Appl. Phys. Lett.* 108 (2016) 132408.
- [60] M. González-Guerrero, J.L. Prieto, D. Ciudad, P. Sánchez, C. Aroca, Engineering the magnetic properties of amorphous (Fe80Co20)80B20 with multilayers of variable anisotropy direction, *Appl. Phys. Lett.* 90 (2007) 162501.
- [61] M. Zimmermann, T.N.G. Meier, F. Dirnberger, A. Kákay, M. Decker, S. Wintz, S. Finizio, E. Josten, J. Raabe, M. Kronseder, D. Bougeard, J. Lindner, C.H. Back, Origin and manipulation of stable vortex ground states in permalloy nanotubes, *Nano Lett.* 18 (2018) 2828–2834.
- [62] D.P. Weber, D. Rüffer, A. Buchter, F. Xue, E. Russo-Averchi, R. Huber, P. Berberich, J. Arbiol, A.F.i. Morral, D. Grundler, M. Poggio, Cantilever magnetometry of individual Ni nanotubes, *Nano Lett.* 12 (2012) 6139–6144.
- [63] C. Rossel, P. Bauer, D. Zech, J. Hofer, M. Willemann, H. Keller, Active microlevers as miniature torque magnetometers, *J. Appl. Phys.* 79 (1996) 8166–8173.
- [64] J.G.E. Harris, D.D. Awschalom, F. Matsukura, H. Ohno, K.D. Maranowski, A.C. Gossard, Integrated micromechanical cantilever magnetometry of  $\text{Ga}_{1-x}\text{Mn}_x\text{As}$ , *Appl. Phys. Lett.* 75 (1999) 1140–1142.
- [65] B.C. Stipe, H.J. Mamin, T.D. Stowe, T.W. Kenny, D. Rugar, Magnetic dissipation and fluctuations in individual nanomagnets measured by ultrasensitive cantilever magnetometry, *Phys. Rev. Lett.* 86 (2001) 2874–2877.
- [66] B. Gross, D.P. Weber, D. Rüffer, A. Buchter, F. Heimbach, A.F.i. Morral, D. Grundler, M. Poggio, Dynamic cantilever magnetometry of individual CoFeB nanotubes, *Phys. Rev. B* 93 (2016) 064409.
- [67] K.A. Modic, M.D. Bachmann, B.J. Ramshaw, F. Arnold, K.R. Shirer, A. Estry, J.B. Betts, N.J. Ghimire, E.D. Bauer, M. Schmidt, M. Baenitz, E. Svanidze, R.D. McDonald, A. Shekhter, P.J.W. Moll, Resonant torsion magnetometry in anisotropic quantum materials, *Nat. Commun.* 9 (2018) 3975.
- [68] P. Banerjee, F. Wolny, D.V. Pelekhanov, M.R. Herman, K.C. Fong, U. Weissker, T. Mühl, Y. Obukhov, A. Leonhardt, B. Büchner, P.C. Hammel, Magnetization reversal in an individual 25 nm iron-filled carbon nanotube, *Appl. Phys. Lett.* 96 (2010) 252505.

- [69] A. Mehlin, F. Xue, D. Liang, H.F. Du, M.J. Stolt, S. Jin, M.L. Tian, M. Poggio, Stabilized skyrmion phase detected in MnSi nanowires by dynamic cantilever magnetometry, *Nano Lett.* 15 (2015) 4839–4844.
- [70] S. Lee, E.W. Moore, S.A. Hickman, J.G. Longenecker, J.A. Marohn, Switching through intermediate states seen in a single nickel nanorod by cantilever magnetometry, *J. Appl. Phys.* 111 (2012) 083911.
- [71] L. Bossoni, P. Carretta, M. Poggio, Vortex lattice melting of a NbSe<sub>2</sub> single grain probed by ultrasensitive cantilever magnetometry, *Appl. Phys. Lett.* 104 (2014) 182601.
- [72] A.C. Bleszynski-Jayich, W.E. Shanks, B. Peaudecerf, E. Ginossar, F. von Oppen, L. Glazman, J.G.E. Harris, Persistent currents in normal metal rings, *Science* 326 (2009) 272–275.
- [73] J. Jang, D.G. Ferguson, V. Vakaryuk, R. Budakian, S.B. Chung, P.M. Goldbart, Y. Maeno, Observation of half-height magnetization steps in Sr<sub>2</sub>RuO<sub>4</sub>, *Science* 331 (2011) 186–188.
- [74] A. Buchter, J. Nagel, D. Rüffer, F. Xue, D.P. Weber, O.F. Kieler, T. Weimann, J. Kohlmann, A.B. Zorin, E. Russo-Averchi, R. Huber, P. Berberich, A.F.i. Morral, M. Kemmler, R. Kleiner, D. Koelle, D. Grundler, M. Poggio, Reversal mechanism of an individual Ni nanotube simultaneously studied by torque and SQUID magnetometry, *Phys. Rev. Lett.* 111 (2013) 067202.
- [75] J. Nagel, A. Buchter, F. Xue, O.F. Kieler, T. Weimann, J. Kohlmann, A.B. Zorin, D. Rüffer, E. Russo-Averchi, R. Huber, P. Berberich, A.F.i. Morral, D. Grundler, R. Kleiner, D. Koelle, M. Poggio, M. Kemmler, Nanoscale multifunctional sensor formed by a Ni nanotube and a scanning Nb nanoSQUID, *Phys. Rev. B* 88 (2013) 064425.
- [76] A. Buchter, R. Wölbing, M. Wyss, O.F. Kieler, T. Weimann, J. Kohlmann, A.B. Zorin, D. Rüffer, F. Matteini, G. Tütüncüoglu, F. Heimbach, A. Kleibert, A.F.i. Morral, D. Grundler, R. Kleiner, D. Koelle, M. Poggio, Magnetization reversal of an individual exchange-biased permalloy nanotube, *Phys. Rev. B* 92 (2015) 214432.
- [77] A. Mehlin, B. Gross, M. Wyss, T. Schefer, G. Tütüncüoglu, F. Heimbach, A.F.i. Morral, D. Grundler, M. Poggio, Observation of end-vortex nucleation in individual ferromagnetic nanotubes, *Phys. Rev. B* 97 (2018) 134422.
- [78] M. Wyss, A. Mehlin, B. Gross, A. Buchter, A. Farhan, M. Buzzi, A. Kleibert, G. Tütüncüoglu, F. Heimbach, A.F.i. Morral, D. Grundler, M. Poggio, Imaging magnetic vortex configurations in ferromagnetic nanotubes, *Phys. Rev. B* 96 (2017) 024423.
- [79] C. Sun, V.L. Pokrovsky, Magnetic properties of a long, thin-walled ferromagnetic nanotube, *J. Magn. Magn. Mater.* 355 (2014) 121–130.
- [80] M. Staňo, S. Schaefer, A. Wartelle, M. Rioult, R. Belkhou, A. Sala, T.O. Menteş, A. Locatelli, L. Cagnon, B. Trapp, S. Bochmann, S. Martin, E. Gautier, J.-C. Toussaint, W. Ensinger, O. Fruchart, Flux-closure domains in high aspect ratio electroless-deposited CoNiB nanotubes, *Sci. Post Phys.* 5 (2018) 038.
- [81] A. Finkler, Y. Segev, Y. Myasoedov, M.L. Rappaport, L. Ne'eman, D. Vasyukov, E. Zeldov, M.E. Huber, J. Martin, A. Yacoby, Self-aligned nanoscale SQUID on a tip, *Nano Lett.* 10 (2010) 1046–1049.
- [82] D. Vasyukov, Y. Anahory, L. Embon, D. Halbertal, J. Cuppens, L. Neeman, A. Finkler, Y. Segev, Y. Myasoedov, M.L. Rappaport, M.E. Huber, E. Zeldov, A scanning superconducting quantum interference device with single electron spin sensitivity, *Nat Nano* 8 (2013) 639–644.
- [83] D. Vasyukov, L. Ceccarelli, M. Wyss, B. Gross, A. Schwab, A. Mehlin, N. Rossi, G. Tütüncüoglu, F. Heimbach, R.R. Zamani, A. Kovács, A.f.i. Morral, D. Grundler, M. Poggio, Imaging stray magnetic field of individual ferromagnetic nanotubes, *Nano Lett.* 18 (2018) 964–970.

- [84] I. Schmid, M.A. Marioni, P. Kappenberger, S. Romer, M. Parlinska-Wojtan, H.J. Hug, O. Hellwig, M.J. Carey, E.E. Fullerton, Exchange bias and domain evolution at 10 nm scales, *Phys. Rev. Lett.* 105 (2010) 197201.
- [85] D. Li, R.S. Thompson, G. Bergmann, J.G. Lu, Template-based synthesis and magnetic properties of cobalt nanotube arrays, *Adv. Mater.* 20 (2008) 4575–4578.
- [86] M. Staňo, Magnetic microscopy of domains and domain walls in ferromagnetic nanotubes, PhD thesis, Université Grenoble Alpes, 2017.